Electrochimica Acta 366 (2021) 137471

Contents lists available at ScienceDirect

Electrochimica Acta

journal homepage: www.elsevier.com/locate/electacta

Synergetic effects of cation (K^+) and anion (S^{2-})-doping on the structural integrity of Li/Mn-rich layered cathode material with considerable cyclability and high-rate capability for Li-ion batteries

Rakesh Saroha [a], Jung Sang Cho [a,*], Jou-Hyeon Ahn [b,*]

[a] Department of Engineering Chemistry, Chungbuk National University, Chungbuk 361-763, Republic of Korea
[b] Department of Materials Engineering and Convergence Technology, Gyeongsang National University, Jinju 52828, Republic of Korea

ARTICLE INFO

Article history:
Received 31 August 2020
Revised 10 November 2020
Accepted 10 November 2020
Available online 13 November 2020

Keywords:
Li-rich cathodes
Cation/anion co-doping
Structural integrity
Lithium-ion batteries

ABSTRACT

Controlling structural deformations and rapid voltage decay during prolonged cycling has been considered the foremost challenge in improving the cycling and rate performance of Li-rich cathode materials for advanced lithium-ion batteries. In this work, we report an effective strategy for delaying structural variations and inhibiting transition metal migration by co-doping with a large-sized cation and anion. A Li-rich layered composite cathode, namely $Li_{1.165}Mn_{0.495}Ni_{0.165}Co_{0.165}O_2$ (LMNCO; $0.5Li_2MnO_3$-$0.5LiMn_{0.33}Ni_{0.33}Co_{0.33}O_2$) was prepared as the starting material, followed by synthesis of the optimized K^+-doped $L_{1.135}K_{0.03}Mn_{0.495}Ni_{0.165}Co_{0.165}O_2$ (LKMNCO) and K^+/S^{2-}-doped $L_{1.135}K_{0.03}Mn_{0.495}Ni_{0.165}Co_{0.165}O_2S_{0.02}$ (LKMNCOS) samples via a co-precipitation method. This co-doping strategy retarded structural deformations by significantly suppressing transition metal migration, as evidenced by ex-situ X-ray diffraction analysis at various cycle numbers for the sample cycled at 1.0 C-rate. The K^+/S^{2-}-doped sample, i.e., LKMNCOS, exhibited exceptional cycling stability and high-rate capability. Owing to the enhanced structural properties, the co-doped sample delivered an initial charge/discharge capacity of 341/295 mAh g^{-1} at 0.05 C, with the lowest irreversible capacity loss (ICL) compared to the pristine and K^+-doped sample. A discharge capacity of ~129 mAh g^{-1} was also achieved even after 450 cycles at 1.0 C-rate, with the highest capacity retention ratio (65%) and lowest average capacity decay rate per cycle (~0.07%), suggesting excellent cycling performance. Overall, the results are prospectively beneficial for further development of advanced layered cathodes that undergo layered-to-spinel transformations and demonstrate the efficacy of co-doping for alleviating undesired structural defects.

1. Introduction

A novel class of Li- and Mn-rich layered transition metal oxides have attracted widespread attention as insertion cathodes for lithium-ion batteries [1,2]. These Li-rich layered oxides, formulated as xLi_2MnO_3-$(1-x)LiMO_2$ or $Li_{1+z}M_{1-z}O_2$ (where M= Mn, Ni, Fe, Co, etc., and $0 < x < 1$, $0 < z \leq 0.33$), have been reported to deliver specific discharge capacities exceeding 250 mAh g^{-1} [1]. This could be attributed to the integrated layered-layered structure formed-between monoclinic Li_2MnO_3 and a rhombohedral $LiMO_2$ phase. The origin of the high discharge capacity of these materials is partially attributed to the participation of redox-active transition metals (Mn, Ni, and Co), and to some extent, oxide ions (O_2^{n-}). A high specific discharge capacity can be obtained after the initial charging reaction, accompanied by the activation of monoclinic Li_2MnO_3, when these materials are charged above 4.5 V *vs.* Li/Li^+. This activation process leads to the removal of lattice oxygen and lithium-ion extraction in the form of Li_2O [$Li_2Mn^{4+}O_3 \rightarrow Mn^{4+}O_2 + Li_2O$] [1]. The irreversible oxygen loss during the initial charge forms oxygen vacancies and triggers a complex mechanism involving migration of the transition metal (TM) ions to the vacant Li sites, eventually causing voltage fading or structural deformation (undesired spinel growth) as cycling proceeds [2]. Such unwanted structural damages result in substandard Li^+-ion diffusion, causing inferior cycling performance and capacity fading during long-term cycling. Good capacity retention and stable voltage responses of the cathode material are crucial factors for maintaining high power and energy densities but are highly challenging to achieve for Li-rich metal oxides.

Substantial effort has been expended in suppressing the voltage fading or structural changes to improve the cycling stability and energy/power density of Li-rich metal oxides over extended cycling. These strategies include novel structural designs

* Corresponding authors.

https://doi.org/10.1016/j.electacta.2020.137471
0013-4686/

[3-8], surface modification using conductive materials [9–16], composite cathodes [17,18], etc. Among the existing approaches, ion-doping is considered as an efficient way to improve the overall cell performance by prohibiting structural changes/damages and effectively alleviating voltage fading/decay. Doping with different foreign ions (cation/anion, co-doping) and their effect on the electrochemical performance have been reported previously [2,19–26]. Doping with alkali metal cations (Na^+, K^+) proved to be more favorable owing to the similarity of the chemical environment of these cations to that of lithium. Ates et al. studied the effect of Na-doping on the rate capability and layered-to-spinel structural transformation of Li-rich cathodes [27]. The group reported that 5 wt-% Na-doping not only improved the conductivity, but also prohibited the layered-to-spinel conversion, which in turn enhanced the rate capability and cycling life. Similarly, Li et al. studied an in-situ K^+-doped Li-rich cathode and reported similar prohibition of the structural transition during cycling [28]. However, the cyclic stability achieved in the reports mentioned above was testified only for a limited number of cycles at either low or high rates. Moreover, the majority of the reported studies are based on single-element doping only (cation-doping in particular) [19,20,29–33]. Therefore, the combined effect of co-doping on the structure and electrochemical properties still needs to be investigated in detail. Although, there are few reports studying the combined effects of doping with other cations and anions on Li-rich cathodes [2,23,24], to the best of our knowledge, there is no report on K^+ and S^{2-} as cation and anion dopants, which prompted us to carry out this investigation.

Inspired by the considerable improvement in the structural transition and rate capability achieved with alkali metal-ion doping, we report an efficient approach involving cation/anion co-doping of a Li/Mn-rich cathode to afford considerable cycling stability and improved electrochemical performance. Herein, potassium and sulfur are selected as the cation and anion, respectively, and a systematic study of their effect on the rate capability, extended cycling stability, and mitigation of the structural transition of the cathode from layered to spinel is executed. The optimized K^+/S^{2-}-doped sample, i.e., $Li_{1.135}K_{0.03}NCMOS_{0.02}$ (LKMNCOS), exhibits exceptional structural stability and enhanced electrochemical performance. Attributed to the robust, reversible layered structure, LKMNCOS delivers a stable discharge capacity of 217.0 mAh g^{-1} at the end of the 80th cycle at 0.1 C-rate. The discharge capacity of ~129 mAh g^{-1} even after 450 cycles at 1.0 C-rate, with the highest capacity retention ratio (65%) and lowest average capacity decay rate per cycle (~0.07%) compared to the pristine and cation-doped samples, suggests the excellent cycling performance of LKMNCOS. The outstanding electrochemical performance of the co-doped sample is ascribed to the exceptional structural stability, leading to hindrance of the layered→ spinel transformation, stable oxygen layer and reduced irreversible capacity loss (ICL), as well as effective mitigation of transition metal migration to the Li sites.

2. Experimental

Chemicals: To synthesize the Li-rich cathodes, analytical grade chemicals, namely, lithium hydroxide monohydrate ($LiOH{\cdot}H_2O$, Sigma-Aldrich, 99.995%), manganese (II) sulfate ($MnSO_4{\cdot}4H_2O$, Sigma-Aldrich, ≥99%), nickel (II) nitrate hexahydrate ($Ni(NO_3)_2{\cdot}6H_2O$), Sigma-Aldrich, ≥98.5%), cobalt (II) nitrate hexahydrate ($Co(NO_3)_2{\cdot}6H_2O$), Sigma-Aldrich, ≥98%), sodium hydroxide pellets (NaOH, Sigma-Aldrich, ≥98%), potassium carbonate (K_2CO_3, Sigma-Aldrich, 99.995%), and lithium disulfide (Li_2S, Sigma-Aldrich, 99.98%) were used as precursor salts without any purification. Deionized (DI) water was used as the solvent to dissolve the sulfate/nitrate salts.

Synthesis of cation/anion stabilized Li/Mn-rich cathodes: All cation/anion stabilized lithium-rich cathodes were synthesized using the conventional co-precipitation technique, followed by high-temperature heating to obtain the pure phase. Briefly, stoichiometric amounts of nitrate/sulfate salts of manganese, nickel, and cobalt were mixed in deionized water and continuously stirred for 2 h at room temperature. Thereafter, NaOH solution as a precipitating agent (4 M) was added dropwise to the above metal salt solution. The pH of the solution was maintained at 10 and stirring was continued for 8 h at room temperature to form uniform metal hydroxide precipitates, followed by vacuum filtration. The filtered metal hydroxide precipitates were dried overnight at 120 °C in a hot air oven to remove moisture and then ground to obtain a fine powder. Thereafter, the powder was mixed with lithium salt using a pestle and mortar and sintered in air at 500 °C for 5 h, followed by calcination at 900 °C for 10 h. Scheme 1 presents a stepwise illustration of the synthesis process. The final lithium-rich pristine material with the composition $Li_{1.165}Mn_{0.495}Ni_{0.165}Co_{0.165}O_2$ ($0.5Li_2MnO_3$-$0.5LiMn_{0.33}Ni_{0.33}Co_{0.33}O_2$), denoted as LMNCO, was stored for further characterization. A series of cation/anion stabilized lithium-rich cathodes were also prepared by a similar approach. Initially, K-doped LMNCO ($L_{1-x}K_xMNCO$; x = 0.01-0.05) samples were prepared. The as prepared metal hydroxide powder was thoroughly mixed with the stoichiometric amount of lithium and potassium precursors followed by the heat-treatment in air at identical conditions as used above. The optimized K-doped LMNCO sample was selected for further sulfur treatment ($L_{1-x}K_xMNCOS_y$; x = 0.03, y =0.01-0.03). Lithium sulfide (Li_2S) was used as a sulfur source. For the synthesis of co-doped samples, metal hydroxide powder was mixed with the stoichiometric amounts of lithium and potassium precursors along with Li_2S and then subjected to heat-treatment in air atmosphere at 500 °C for 5 h and 900 °C for 10 h. The synthesized samples were stored in a vacuum oven at 60 °C for further analysis.

Physical characterization: Crystal structure and phase analyses of the as-synthesized samples were performed using a Bruker X-ray diffractometer (D2 Phaser Bruker AXS) with $CuK_{\alpha 1}$ radiation (1.5405 Å) in the 2θ range of 10–70° with a step size of 0.02°. Rietveld refinement of the XRD data was performed for all optimized samples. Note that no data smoothening and background subtraction was performed before plotting. The morphological and surface properties of the prepared samples were examined using a Philips field- emission scanning electron microscope (FE-SEM, XL30S FEG, operating at 15 kV) equipped with an energy dispersive X-ray (EDX) analyzer for elemental mapping. Elemental compositions of the as-prepared powders were also analyzed using inductively coupled plasma atomic emissions spectroscopy (ICP-AES). Thermogravimetric (TG) analysis was carried out for precursor powders of optimized undoped, cation, and co-doped sample in O_2 atmosphere at a ramp rate of 10 °C min^{-1}. X-ray photoelectron microscopy (XPS) studies were carried out to determine the oxidation state of manganese, cobalt, nickel, and potassium using a monochromatic Al-Kα X-ray source.

Electrode preparation and electrochemical measurements: Stainless steel Swagelok® cells were assembled to study the electrochemical performance of the synthesized samples. Electrodes were prepared by the slurry coating technique using the prepared powders, super P, and polyvinylidene fluoride (PVDF) binder mixed in a weight ratio of 8:1:1 in the minimum amount of *N*-methyl-2-pyrrolidone (NMP). The slurry was then coated on Al-foil, dried overnight at 120 °C in air, and roll pressed. Circular electrodes (ϕ =10 mm) were cut with an average loading of ~4 mg cm^{-2}, followed by heating at 60 °C for 1 h, and subsequently transferred to an argon-filled glovebox. The electrolyte used was 1 M $LiPF_6$ in EC/DEC (1:1 v/v). Galvanostatic charge/discharge and cyclic voltammetry tests were conducted using a WBCS3000 bat-

tery cycler (WonATech) at room temperature. The voltage window for the electrochemical measurements was fixed at 2.0-4.8 V. Impedance measurements were performed using an impedance analyzer (ZIVESP2 Electrochemical Workstation) in the frequency range of 2 MHz to 0.01 Hz with a 5 mV AC wave amplitude. The galvanostatic intermittent titration technique (GITT) was performed at a current pulse equivalent to 0.1 C for 30 min, followed by a relaxation of 2 h to calculate the lithium-ion diffusion coefficient (D_{Li+}). The C-rate was calculated by equating 1C = 230 mAh g^{-1}. For the ex-situ XRD studies, stainless steel Swagelok® cells were transferred to glovebox after charge/discharge, and the electrodes were removed carefully, followed by drying at 50 °C. Subsequently, the dried electrodes were placed inside a sample holder covered with a glass lid for X-ray diffraction studies.

3. Results and discussion

3.1. Crystal structure of synthesized samples

The pristine, K^+-doped, and K^+/S^{2-}-doped samples were prepared using the co-precipitation method followed by two-step heat-treatment. The detailed procedure for formation of the nanostructure is illustrated in Scheme 1. Thermogravimetric (TG) measurement of precursor powders was performed initially for optimized undoped, cation, and co-doped samples to evaluate the phase change process during the thermal treatment and the obtained results are shown in Fig. S1. The obtained TG curves primarily consist of four weight loss regions where region I (30–100 °C) represents weight loss mainly due to the removal of moisture or adsorbed water molecules. A massive weight loss took place in region II between 100-450 °C, which is mainly originated due to the decomposition of oxygen-containing groups [34]. The further weight loss associated with cation and co-doped sample in region III (450-700 °C) is associated with the decomposition of metal salts, which is almost constant for undoped sample, suggesting onset of doping process. Furthermore, the minor weight loss in region IV (>700 °C) is observed, which indicates the formation of metal oxide structure. No further weight loss was observed above 850 °C suggesting the formation of lithium-rich pure phase. The phase purity and crystal structure of the synthesized samples was confirmed by X-ray diffraction analysis (Fig. 1(a,b)). The narrow and intense peaks for all the Li-rich layered-oxide samples indicate a high degree of crystallinity (Fig. 1a and 1b). The diffraction peaks could be indexed to the hexagonal α-$NaFeO_2$ unit cell with *R-3m* symmetry, while the weak and broad diffraction peaks around 20-25° (Fig. S2) are attributed to the superlattice structure (i.e., Li and Mn ordering in the transition metal layers) of the Li_2MnO_3 component in the integrated composite cathode [1,27,35]. Besides, even after cation (K^+) doping (Fig. 1(a)), the XRD profiles showed no secondary and/or impurity phases, thus indicating the phase purity of the synthesized samples. To further elucidate the influence of doping with larger cation ion doping (K^+) on the structural changes of the pristine material (LMNCO), the highly intense diffraction peaks of the (003) and (104) planes were magnified, as shown in Fig. 1(a1) and (a2), respectively. As shown in Fig. 1(a1), the (003) peak shifted to a lower 2θ angle with K^+-doping, indicating an increase in the cell volume due to expansion of the interplanar spacing. This suggests that the larger potassium ion was successfully doped into the pristine material, resulting in expansion along the c-axis, which may be favorable for better Li^+ conduction. The apparent splitting of the (018) and (110) peaks around $2\theta = 65°$ suggests that all of the synthesized samples possess a highly ordered, well-defined layered structure without any secondary phases. The intensity ratio of the two major peaks, i.e., $I_{(003)}/I_{(104)}$, was calculated for the K^+-doped samples (Table 1). It has been reported that in the absence of cation disordering, the intensity ratio must exceed 1.2 [36]. The intensity ratio, was high for the pristine and K^+-doped samples, indicating low cation disordering. Among the K^+-doped samples, the $I_{(003)}/I_{(104)}$ ratio was highest for $Li_{1.135}K_{0.03}MNCO$ (i.e., 1.63), suggesting the absence of cation disordering. In addition, for samples of high doping content, such as $L_{1.115}K_{0.05}MNCO$, the shift to a lower 2θ for (003) peak is less than for other K^+-doped samples. It might be due to unfavorable cation arrangement caused by high doping content which is clearly evident from the lowest $I_{(003)}/I_{(104)}$ ratio value. Based on the XRD pattern and intensity ratio $(I_{(003)}/I_{(104)})$, $Li_{1.135}K_{0.03}MNCO$ was selected for further anion (sulfur) treatment. The XRD results (Fig. 1b) confirmed that the hexagonal α-$NaFeO_2$ unit cell with *R-3m* symmetry was preserved in the cation (K^+) and anion (S^{2-})-doped samples, without any impurity or secondary phase. Moreover, the intensity ratios $(I_{(003)}/I_{(104)})$ values indicate that the cation disordering decreased with sulfur treatment, with almost identical values (i.e., 1.74) for the $Li_{1.135}K_{0.03}MNCOS_{0.020}$ and $Li_{1.135}K_{0.03}MNCOS_{0.025}$ samples, thus indicating the lowest cation mixing. Therefore, these results suggest that co-doping may be a valuable strategy for obtaining superior crystal structures, leading to enhanced electrochemical performances. To further elucidate this, the cycling performance of all synthesized samples was initially evaluated at 0.1 C-rate to determine the optimal composition of the cation and cation/anion-doped samples, as shown in Fig. S3(a, b). As demonstrated, among the K^+-doped samples, $Li_{1.135}K_{0.03}MNCO$ exhibited the highest and stable discharge capacity for 50 continuous charge-discharge cycles. Similarly, among the K^+/S^{2-}-doped samples, $Li_{1.135}K_{0.03}MNCOS_{0.020}$ displayed the highest discharge capacity over 80 cycles. Although, the cycling performance of the $Li_{1.135}K_{0.03}MNCOS_{0.020}$ and $Li_{1.135}K_{0.03}MNCOS_{0.025}$ samples was very similar, based on the cycling stability, $Li_{1.135}K_{0.03}MNCOS_{0.020}$ was selected as the optimal sample among the co-doped samples. The obtained cycling performance is in good agreement with the XRD results. Henceforth, only pristine LMNCO, K^+-doped $Li_{1.135}K_{0.03}MNCO$, and the K^+/S^{2-}-doped $Li_{1.135}K_{0.03}MNCOS_{0.02}$ sample are considered for further analysis and electrochemical characterization. Hereafter, the optimal K^+-doped ($Li_{1.135}K_{0.03}MNCO$) and co-doped sample ($Li_{1.135}K_{0.03}MNCOS_{0.02}$) are abbreviated as LKMNCO and LKMNCOS, respectively.

To determine the lattice dimensions of the layered oxides and validate the XRD results, Rietveld refinement of the XRD data for the optimized samples was carried out. XRD refinements were performed using the R-3m ($LiMn_{0.2}Ni_{0.2}Co_{0.6}O_2$, JCPDS: 01-074-8968) and C2/m (Li_2MnO_3: JCPDS: 01-084-1634) space group and the obtained refinement profiles, along with the refined lattice parameters, are presented in Fig. 2 and Table 2. As listed in the refinement Table 2, a monotonic increase in the c-axis values was clearly evident, indicating an increase in the unit cell volume after K^+-doping, suggesting that the K dopant was primarily localized in the Li-layers. The obtained refinement results are in good accordance with the XRD results, suggesting that K-doping should facilitate better Li-ion conduction through the enlarged interlayer spacing.

3.2. Morphology and valence state analysis of synthesized samples

The morphologies of the as-prepared samples were observed using FE-SEM (Fig. 3). As observed, the synthesized samples revealed the formation of nanosized particles. Moreover, compared to the pristine LMNCO sample, the particles in K^+ and K^+/S^{2-}-doped samples were more uniformly dispersed, homogenously distributed, and less aggregated, which could be beneficial for better electrolyte percolation and lithium diffusion. The average particle size was ~200 nm for the synthesized samples. Elemental mapping was used to evaluate the element distribution in the synthesized

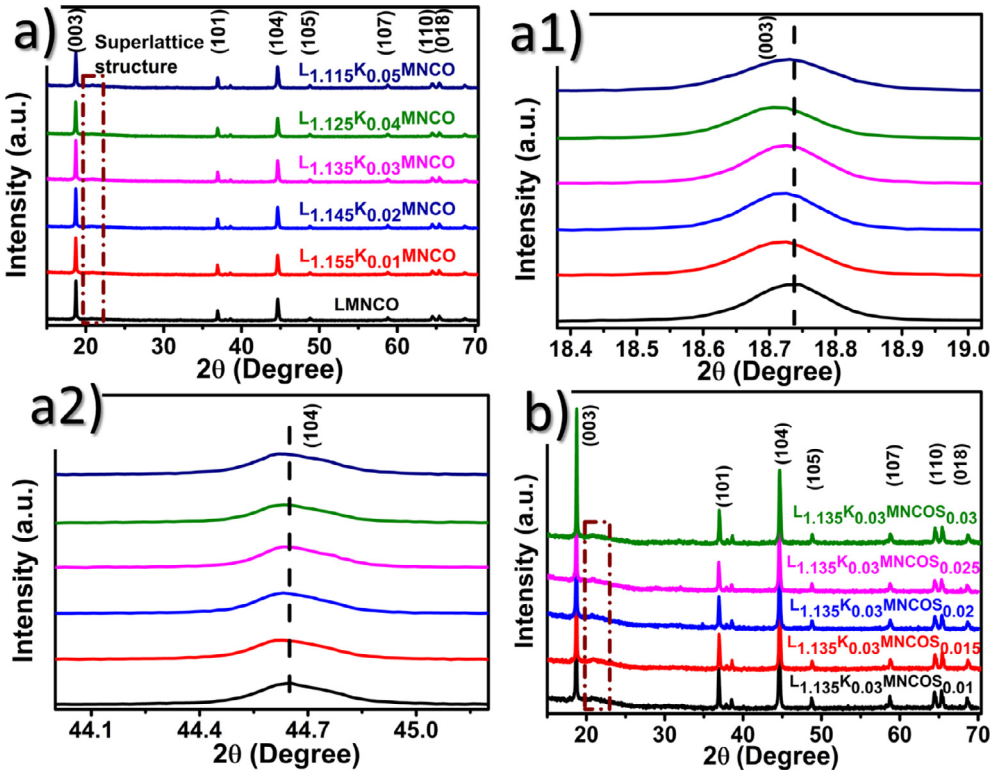

Fig. 1. X-ray diffraction (XRD) patterns of as-prepared compositions: (a) $L_{1-x}K_xMNCO$; x= 0.01-0.05 and (a1, a2) corresponding magnified view of peak (003) and (104), respectively, and (b) XRD patterns of co-doped $L_{1-x}K_xMNCOS_y$; x= 0.03, y=0.01–0.03 samples.

Table 1
Comparison of respective intensity ratio values of two major peaks [$I_{(003)}/I_{(104)}$] for all the synthesized compositions.

Sample	(I_{003}/I_{104})	Sample	(I_{003}/I_{104})
LMNCO	1.53	$L_{1.135}K_{0.03}MNCO$	1.63
$L_{1.155}K_{0.01}MNCO$	1.57	$L_{1.135}K_{0.03}MNCOS_{0.01}$	1.63
$L_{1.145}K_{0.02}MNCO$	1.58	$L_{1.135}K_{0.03}MNCOS_{0.015}$	1.67
$L_{1.135}K_{0.03}MNCO$	1.63	$L_{1.135}K_{0.03}MNCOS_{0.02}$	1.73
$L_{1.125}K_{0.04}MNCO$	1.58	$L_{1.135}K_{0.03}MNCOS_{0.025}$	1.74
$L_{1.115}K_{0.05}MNCO$	1.41	$L_{1.135}K_{0.03}MNCOS_{0.03}$	1.56

Table 2
Rietvield refined crystal structure parameters for optimized compositions. Digits in the bracket denotes the error in the repective numeric value.

Sample	Lattice constants a (Å)	b (Å)	c (Å)	V (Å^3)	c/a ratio	Refinement parameters
LMNCO	2.84861(3)	2.84861(3)	14.23465(6)	100.033(2)	4.99705	R_{wp}: 3.90; R_p: 3.13; χ^2: 7.98
LKMNCO	2.84918(4)	2.84918(4)	14.24055(2)	100.155(2)	4.99812	R_{wp}: 3.97; R_p: 3.24; χ^2: 8.065
LKMNCOS	2.85012(5)	2.85012(5)	14.24576(4)	100.416(6)	4.99830	R_{wp}: 5.68; R_p: 4.67; χ^2: 7.48

compositions. Fig. 3(a1–a4, b1–b5, and c1–c6) shows that all elements (Mn, Ni, Co, K, S, and O) were homogeneously distributed in the optimized samples. Additionally, the approximate composition was obtained using EDS element analysis, as shown in Fig. S4(a–c) and corresponding Table. The derived chemical compositions are in good agreement with the original compositions (ignoring the permitted error of the EDS tests), indicating high integrity of the elements in the samples. However, the slightly lower amount of potassium in the approximated compositions could be attributed to K^+-loss at high sintering temperature. In addition, the elemental composition of the optimized Li-rich cathodes was also obtained from inductively coupled plasma atomic emission spectrometry (ICP-AES), as shown in Table T1. The atomic ratio of all the elements matches fairly with the target value.

X-ray photoelectron spectroscopy (XPS) was used to evaluate the valence state of the component elements in the synthesized samples. Fig. S5(a–d) shows the magnified XPS profiles corresponding to the Mn 3s, Co 2p, Ni 2p, C 1s, and K 2p regions, while the survey spectrum for the optimized samples is presented in Fig. S6(a). As indicated in the XPS profiles, the photoelectron signals of the respective transition metal ions were almost identical for the synthesized samples. For the three samples, the binding energy values corresponding to the Mn 3s doublet were ~84.0 (Mn 3s ^{7}S) and 88.3 eV (Mn 3s ^{5}S) and could be related to the interaction between unpaired 3s electron with parallel (^{7}S) and antiparallel spin (^{5}S) with the unpaired 3d electrons [37,38]. The separation between these doublets (Δ = 4.35 eV) indicates the presence of only the Mn^{4+} oxidation state and therefore the exclusion of Mn^{3+} [28]. Additionally, Mn 2p photoelectron signals were also recorded for all samples (Fig. S6(b)), which exhibited high intensity signals around 642.2 eV (Mn 2p3/2) and 653.40 eV (Mn 2p1/2), confirming the presence of Mn^{4+} species as a major constituent again [39]. Similarly, binding energies of 779.5, 794.4, 854.3, and 871.7 eV were obtained for Co 2p3/2, Co 2p1/2, Ni 2p3/2, and Ni 2p1/2, respectively, in good agreement with the previous report, indicating the presence of Co^{3+} and Ni^{2+} [40–42]**.** However, the C 1s and K 2p spectra illustrate a noticeable difference in the binding energy range of 280–297 eV. In particular, the profile of the K^+-doped samples, i.e., LKMNCO and LKMNCOS, showed strong peaks at binding energies higher than 290 eV. The doublet observed at 292.3 and 295.3 eV for K 2p3/2, and K 2p1/2, respectively, was absent in the profile of the pristine LMNCO sample, indicating successful potassium doping [28]. Moreover, the C 1s peak at 284.3 eV remained unchanged, suggesting a similar carbon environment in the three samples. The S 2p XPS data was also recorded for the LKMNCOS sample to examine the nature of sulfur in the synthesized sample, and the results are shown in Fig. S6(c). The peaks at 161.8 and 160.9 eV are associated with bridging sulfur and terminal sulfur, respectively, while the peak at binding energies higher than 167.0 eV could be assigned to oxidized sulfur species [43]. These results clearly indicate the presence of the sulfur atom, along with other transition metal ions, in the synthesized structure. Overall, the XPS results suggest that the valence state of the transition metal ion remains unchanged in all the synthesized samples.

3.3. LKMNCOS as a robust cathode

To better understand the electrochemical redox reactions of these three optimized samples, the cyclic voltammetry (CV) curves were recorded for the initial ten cycles. Fig. 4(a–c) shows the cyclic voltammetry (CV) curves of the synthesized samples, acquired at 0.1 mV s^{-1} in the voltage window of 2.0–4.8 V, at room temperature. During the initial scan, all optimized samples displayed similar CV behavior with a slight difference in the current values. For instance, the peak around 4.1 V in the anodic scan for all samples, is primarily associated with the oxidation of Ni^{2+}/Co^{3+} to Ni^{4+}/Co^{4+} in the layered structure [44–47]. The anodic peak at 4.6 V is mainly correlated with Li_2O extraction from the Li_2MnO_3 component of the synthesized samples [1,48]. The intensity of this peak increased in succession for the pristine to K^+-doped and the K^+/S^{2-}-doped sample, indicating a monotonic increase of the initial charge capacity. During the initial cathodic scan, no cathodic peaks were observed at 4.6 V, indicating irreversible electrochemical activation of the Li_2MnO_3 component. Furthermore, the cathodic peaks observed around 3.7 and 3.2 V are ascribed to the reduction of Ni^{4+}/Co^{4+} to Ni^{2+}/Co^{3+} and Mn^{4+} to Mn^{3+}, respectively. However, the absence of the Mn^{3+}/Mn^{4+} oxidation peak during the initial scan for the as-prepared samples clearly suggests that the Mn^{4+} species remains electrochemically inactive. However, after the first scan, a minor Mn^{3+}/Mn^{4+} oxidation peak appeared in the profile of the pristine and K^+-doped samples, i.e., LMNCO and LKMNCO samples, but was absent for the K^+/S^{2-}-doped sample (LKMNCOS). The presence of inactive Mn^{4+} species in the samples is believed to stabilize the layered structure but with lower or gradual capacity fading over cycling due to the complete activation of Li_2MnO_3 during the initial cycle (as discussed later). How-

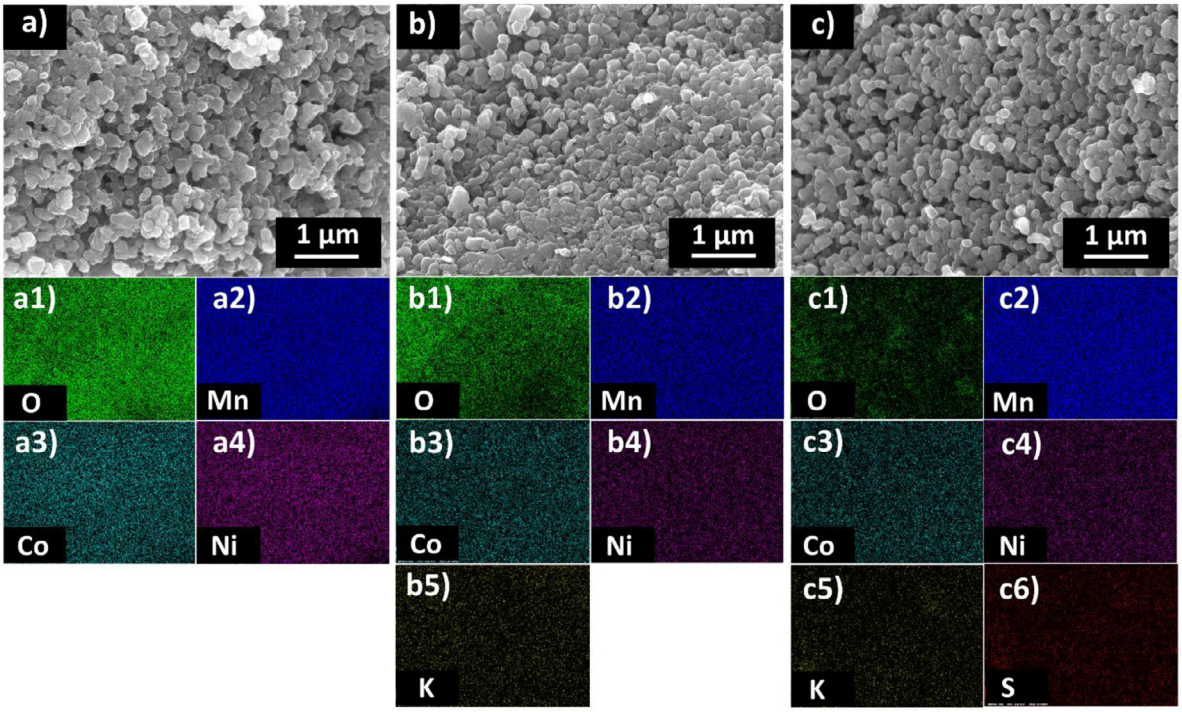

Fig. 3. FE-SEM images of optimized compositions: (a) Pristine LMNCO, (b) LKMNCO, and (c) LKMNCOS. (a1–a4) Respective elemental mapping for LMNCO, (b1–b5) corresponding elemental mapping for LKMNCO, and (c1–c6) elemental mapping for LKMNCOS sample.

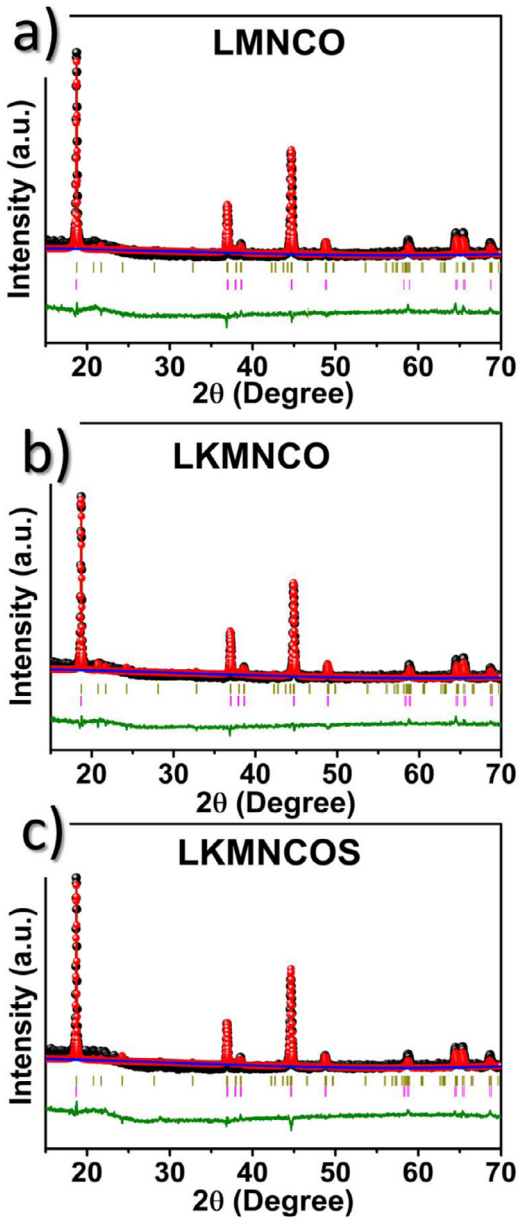

Fig. 2. Rietveld refined XRD profiles of (a) Pristine LMNCO, (b) LKMNCO, and (c) LKMNCOS obtained using R-3m and C2/m space group for $LiMn_{0.33}Ni_{0.33}Co_{0.33}O_2$ and Li_2MnO_3, respectively. Experimental, fitted, background, and difference profiles are shown by black sphere, red sphere, blue line, and green line, respectively. The vertical ticks above the difference profile marks the Bragg position (Dark yellow: C2/m and Pink: R-3m) (For interpretation of the references to color in this figure legend, the reader is referred to the web version of this article.).

ever, for better evaluation of the structural stability, the ratio of the oxidation peak current, i.e., $I_p(4.6\ V)/I_p(4.1\ V)$, was determined. It was previously reported that a lower peak ratio value indicates a highly stable structure [44]. The values corresponding to LMNCO, LKMNCO, and LKMNCOS were 2.123, 1.980, and 1.897, respectively, indicating that the K^+/S^{2-}-doped sample underwent less structural changes and possessed superior cycling stability. The observation of the Mn^{3+}/Mn^{4+} oxidation peak after the first scan for the co-doped sample indicates the presence of Mn^{4+} active species, with a gradual increase in the intensity over cycling, which suggests incomplete activation of Li_2MnO_3 during the initial cycle. This process induces a gradual increase in the capacity and/or stable cyclability over prolonged cycling. After the first cycle onwards, more stable and overlapped CV curves were obtained with slight perturbations. For instance, the electroactivity of the nickel redox couple was found to decrease during the initial few cycles for all samples, and finally stabilized with further cycling. Overall, the CV curves envisaged better electrochemical performance and lithium-ion kinetics for the K^+/S^{2-}-doped sample as compared to the pristine and K^+-doped samples. The obtained CV results are also in good agreement with the XRD analysis (Fig. 1).

In order to understand the effect of cation (K^+) and anion (S^{2-}) doping on the electrochemical performance, the initial charge-discharge curves were recorded at 0.05 C-rate (1C = 230 mAh g^{-1}) as shown in Fig. 4d. As predicted from the CV curves, all samples exhibited a smooth voltage increase in the 3.75 – 4.45 V range, followed by a stable voltage plateau with a voltage higher than 4.45 V, and finally a sloppy voltage profile when charged further above 4.6 V to 4.8 V. The smooth voltage profile in the 3.75 – 4.45 V region can be attributed to lithium deinsertion from the layered-type $Li[M]O_2$ (M = transition metal) framework, while the long voltage plateau around 4.5 V may be related to activation of the Li_2MnO_3 component in the composite through Li_2O extraction. The optimized samples displayed slightly different behavior in the 4.45 – 4.6 V range, indicating marginally different redox reactions. For example, the voltage plateau was relatively longer for the K^+/S^{2-}-doped sample than for the undoped and K^+-doped samples, suggesting a larger initial charge capacity. The initial charge-discharge capacities of the as-prepared LMNCO, LKMNCO, and LKMNCOS samples were 293/239, 322/272, and 341/291 mAh g^{-1}, respectively, with initial Coulombic efficiencies of 81.5, 84.4, and 85.3 %. The higher Coulombic efficiency for the co-doped sample clearly suggests a decrease in the irreversible capacity loss (ICL) for the K^+/S^2-doped sample compared to other two samples. This result is more pronounced considering the voltage polarization values for all optimized samples. For instance, the LKMNCOS sample showed the lowest voltage polarization (ΔV = 0.95 V) among the three prepared samples, suggesting improved redox reaction kinetics. The discharge voltage shifted gradually (mid ΔV = 0.142 V) towards higher potential (highlighted in green), from pristine LMNCO to LKMNCOS, indicating that the robustness of the structure increased, with enhanced electrochemical thermodynamics. For better evaluation of the structural integrity of the LKMNCOS sample, the differential capacity (*dQ/dV*) versus voltage curves corresponding to the charge-discharge at 0.05 C-rate were obtained and analyzed. Fig. 4e reveals the change in *dQ/dV* profiles for three optimized samples. As observed, the intensity of the oxidation peak around 4.0 V and 4.6 V increased monotonically from pristine to K^+/S^{2-}-doped samples, suggesting that redox kinetics was better than other two samples. These observations, along with the CV curves, lead us to conclude that the K^+/S^{2-}doping not only suppressed oxygen vacancies during the initial charge-discharge cycle, but also enabled better utilization of Mn, leading to enhanced electrochemical performance compared to the other prepared samples.

To further investigate the feasibility and advantage of the co-doped sample for more practical applications, stepwise rate capability tests were performed at different C-rates ranging from 0.1 – 7.0 C (Fig. 4f). The charge/discharge capacities corresponding to the K^+/S^{2-}-doped sample i.e., LKMNCOS, were 262/246, 231/218, 207/188, 173/155, 144/129, 110/93, and 81/80 mAh g^{-1} at 0.1, 0.2, 0.5, 1.0, 2.0, 5.0, and 7.0 C-rate, respectively. On the other hand, the charge/discharge capacities for LMNCO and LKMNCO were 243/226, 214/202, 189/173, 162/146, 133/116, 72/63, 47/45, and 249/235, 231/219, 207/191, 179/163, 150/136, 84/71, 52/55, respectively, at identical C-rates. Moreover, when the current was reversed, the original capacity of the co-doped sample was almost fully recovered at 0.1 C, thus indicating excellent capacity retention and rate capability. Table 3 compares the respective discharge capacity retention ratios for the three optimized samples at each C-rate with respect to 0.1 C. As observed, LKMNCOS displayed good capacity

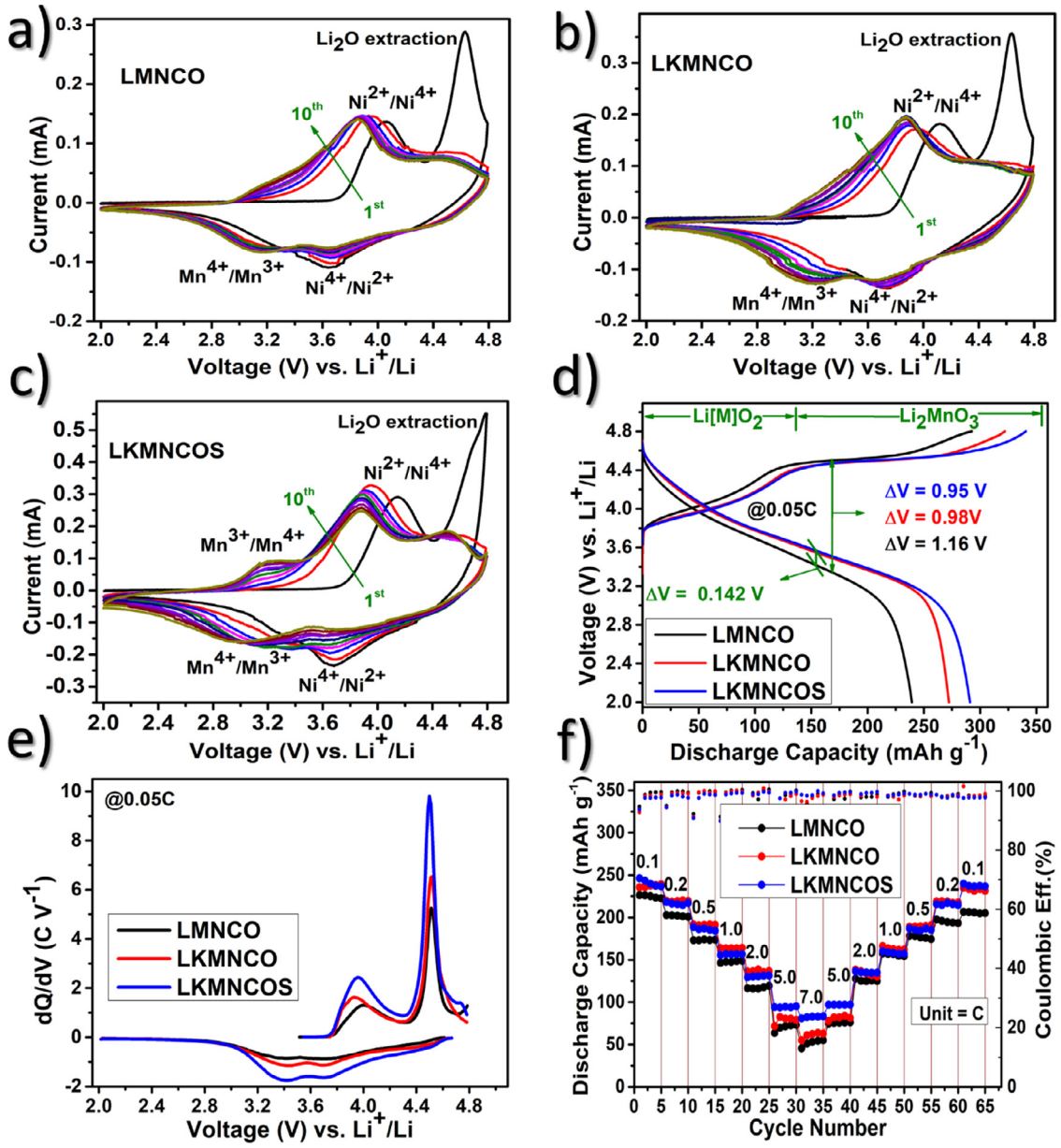

Fig. 4. Electrochemical performances of as-prepared samples. (a–c) CV curves of LMNCO, LKMNCO, and LKMNCOS samples for initial 10 cycles at a scan rate of 0.1 mV s^{-1}, (d) Initial charge -discharge process at 0.05 C for optimized samples, (e) Corresponding differential capacity versus voltage curves at 0.05 C-rate, (f) Rate performance at various C-rates (0.1 – 7.0 C). C-rates were determined by equating 1C to 230 mAh g^{-1}.

retention (percentage), particularly at high C-rates of 5.0 and 7.0 C, compared to the other two samples, which clearly reflects the structural superiority of the co-doped sample. Additionally, the loss of the discharge capacity at high current rates could be attributed to the large polarization effects, which were more pronounced in the undoped and K^+-doped samples, as indicated by the corresponding charge-discharge profiles at each C-rate (Fig. S7(a–c)). The outstanding rate capability of the K^+/S^{2-}-doped sample can be ascribed to the robust layered structure with minimal variations, along with the enlarged interlayer spacing, leading to fast lithium-ion and electron kinetics during the charge-discharge process, compared with the other two samples.

The cycling performance is the foremost benchmark for evaluating the commercial applicability of synthesized compositions for LIB applications. Fig. 5a displays the cycling performance data for the optimized cathodes at 0.1 C-rate. The initial discharge capacity of LMNCO, LKMNCO, and LKMNCOS was 244, 248, and 232 mAh g^{-1}, with an initial Coulombic efficiency of 96.9, 98.3, and 99.7%, respectively. However, after 25 cycles, the discharge capacity of LMNCO decreased sharply to 192 mAh g^{-1} compared to 231 and 239 mAh g^{-1} for LKMNCO and LKMNCOS, respectively, suggesting irreversible structural changes leading to fast capacity fading, as illustrated by the CV curves. With continued cycling, the discharge capacity of the K^+-doped sample, i.e., LKMNCO, decreased, reaching 215 mAh g^{-1} after the 50th cycle, indicating that structural changes were still prominent in the cation-doped sample, but were delayed to some extent. On the other hand, the discharge capacity of the K^+/S^{2-}-doped sample, i.e., LKMNCOS, was 224 mAh g^{-1} and decreased only slightly even after the 80th charge-discharge cycle (217 mAh g^{-1}). Therefore, the stable cycling performance at 0.1 C-rate clearly indicates that cation and anion doping not only prohibits the structural deformation process during extended cycling, but also provides enlarged channels for faster lithium-ion transport. The higher Coulombic efficiency (>98.0 %) also indi-

Table 3
Elecetrochemical performance comparison of optimized samples at various C-rates and cyclic capability at 1.0 C-rate.

Samples	R[a] (%) 0.1 C (mAh g^{-1})	0.2 C	0.5 C	1.0 C	2.0 C	5.0 C	7.0 C	1.0 C (mAh g^{-1}) 1st	Last	R[b] (%)
LMNCO	226.3	89.6	76.5	64.6	58.9	32.1	20.8	178.3	115.1[#]	64.5
LKMNCO	235.7	93.2	81.2	69.5	57.7	30.4	23.3	185.5	111.5[@]	60.1
LKMNCOS	246.3	88.6	76.5	63.1	52.5	38.1	32.8	197.9	128.8[$]	65.0

[a] capacity retention ratio of prepared samples compared to 0.1 C.
[b] capacity retention ratio of prepared samples compared to 1st cycle at 1.0 C.
[#] 200th;
[@] 300th;
[$] 450th

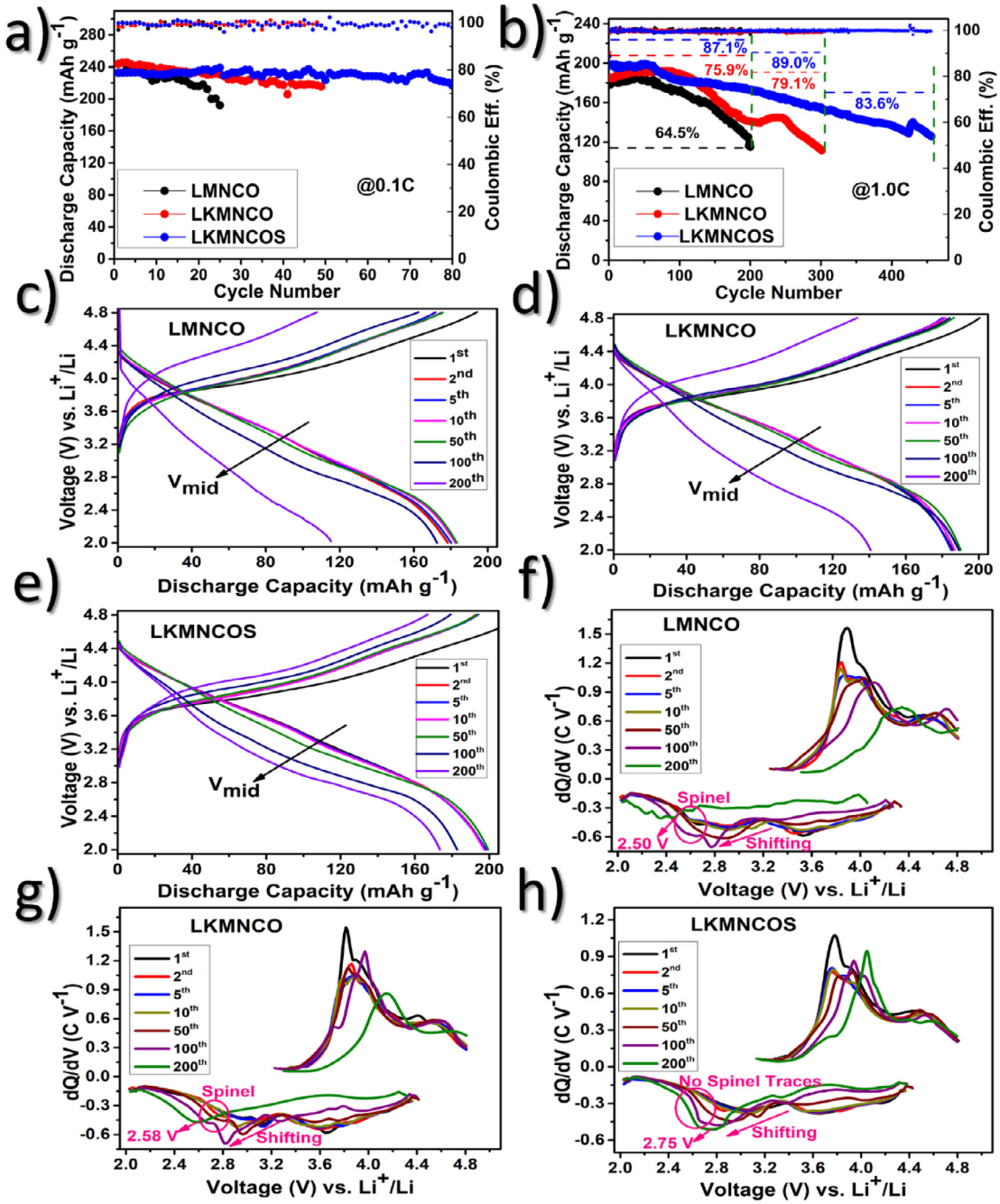

Fig. 5. Cycling performance results of the optimized samples. (a) Cycling performance at 0.1 C-rate, (b) Prolonged cycling results of all the samples at 1.0 C-rate, (c–e) Charge-discharge voltage profiles at various cycle number for optimized samples at 1.0 C-rate, and (f–h) corresponding differential capacity (dQ/dV) versus voltage plots at different cycle number.

cates the structural integrity and high reversibility of the LKMNCOS sample during prolonged cycling. Fig. 5b shows the long-term cycling stability of the optimized samples at 1.0 C-rate. As observed, the initial discharge capacity of the undoped LMNCO and K^+-doped LKMNCO samples was 178 and 186 mAh g^{-1}, respectively. However, with continued cycling, the discharge capacity of pristine LMNCO decreased sharply to 115 mAh g^{-1} after 200 cycles (only 64.5% retention), while for LKMNCO, the discharge capacity was around 141 mAh g^{-1} (~76% capacity retention). On the other hand, the K^+/S^{2-}-doped sample, i.e., LKMNCOS, delivered an initial discharge capacity of 198 mAh g^{-1} and retained a value of 172 mAh g^{-1} after 200 cycles, indicating much higher capacity retention(~87%) compared to the other two samples. Furthermore, after 300 continuous charge-discharge cycles, LKMNCOS still displayed a higher capacity retention (~89%) than the LKMNCO sample (~79%), indicating better lithium-ion transport. Even after 450 cycles, co-doped LKMNCOS delivered a discharge capacity of ~129 mAh g^{-1}, thus suggesting excellent cycling performance. Table 3 displays the capacity retention ratio of all three samples for better comparison. Even after prolonged cycling, the capacity retention ratio of K^+/S^{2-}-doped sample was the highest (65%) among the optimized samples. The average capacity decay rate per cycle was lowest for the co-doped sample (~0.07% per cycle) compared to that of the other two synthesized samples (~0.18% and 0.13% for undoped and K^+-doped samples, respectively). The electrochemical performance obtained in the present work is either comparable or superior to that of other co-doped Li-rich cathodes reported previously (Table T2). These results indicate that co-doping is highly effective for improving the structural stability and minimizing structural variations, leading to outstanding electrochemical performance.

For better comparison, the LMNCO sample doped with sulfur only ($LMNCOS_{0.02}$) was also prepared. Fig. S8(a-e) shows the structural and electrochemical characterization results of the $LMNCOS_{0.02}$ sample. As observed, the FE-SEM micrograph (Fig. S8a) reveals the formation of homogeneously distributed nanoparticles with an average particle size of about 200 nm. Besides, a slight agglomeration is also evident from the FE-SEM image. The crystal structure was confirmed by XRD pattern as shown in Fig. S8b. The sharp and intense peaks in the XRD pattern could be indexed to the hexagonal α-$NaFeO_2$ unit cell with *R-3m* symmetry with low intensity diffraction peaks around 20-22° are also observed that could be linked to the Li and Mn ordering as discussed in the Section 3.1. Moreover, the intensity ratio of the two major peaks, i.e., $I_{(003)}/I_{(104)}$, was observed around 1.61, which suggests that the cation ordering in the sample is better than the pristine LMNCO sample but lower than either of the cation (LKMNCO) and/or cation-anion (LKMNCOS) doped sample. To determine the electrochemical performance, rate capability tests were conducted for the $LKMNCOS_{0.02}$ sample at various C-rates ranging from 0.1-7.0 C as shown in Fig. S8c. The assembled cell was initially charge-discharge at 0.05 C. The initial discharge capacity values were found to be around 244, 234, 213, 182, 150, 109, 53, and 43 mAh g^{-1} at 0.05, 0.1, 0.2, 0.5, 1.0, 2.0, 5.0 and 7.0 C-rate, respectively. The corresponding voltage profiles at various C-rates is shown in Fig. S8d. The observed rate performance reveals that purely sulfur-doping improves the electrochemical performance at low C-rates (0.1, 0.2, and 0.5 C). However, at high C-rates, $LMNCOS_{0.02}$ sample exhibits discharge capacity values similar to the pristine LMNCO sample. To gain further insights, cycling performance was conducted at 0.1 and 1.0 C-rate as shown in Fig. S8e. As observed, $LMNCOS_{0.02}$ delivers an initial discharge capacity of about 226/163 mAh g^{-1} at 0.1/1.0 C, respectively. The discharge capacities at 0.1 C-rate decreases marginally even after more than 60 charge-discharge cycles, while at 1.0 C-rate, the sample tends to deliver lower discharge capacities. The $LMNCOS_{0.02}$ delivers a discharge capacity of around 220 mAh g^{-1} after 67^{th} cycle at 0.1 C while a discharge capacity value of 134 mAh g^{-1} after 120th cycle was observed which is lower compared to the K^+/S^{2-}-doped sample (LKMNCOS). The low capacity values during prolonged cycling could be attributed to the sluggish redox kinetics possibly arises from small interlayer spacing compared to the co-doped sample. These results show that the cation and anion co-doping strategy is far more effective in enhancing the electrochemical performance than only cation or anion-doping

The variation in the average discharge voltage over cycling for all three optimized samples at 1.0 C-rate is shown in Fig. S9. For the LMNCO sample, the average discharge voltage decreased from 3.24 V to 3.03 V after 200 continuous cycles, whereas for LKMNCO, the average discharge voltage dropped from 3.35 V to 3.09 V over 300 cycles. The slow voltage fading in the K^+-doped sample may be attributed to the large interlayer spacing and robust layered structure despite repeated cycling. However, structural changes during cycling still occurred in both samples, as evident from the corresponding charge-discharge profiles presented in Fig. 5(c–e). The gradual shift in the mid voltage (V_{mid}) was more prominent for the undoped sample than the cation-doped sample, as expected. However, this voltage shift towards low values was delayed to some extent for the LKMNCO sample, suggesting minimal structural variations. In contrast, the average discharge voltage of the LKMNCOS sample was reduced from 3.36 V to 3.10 V over more than 450 charge-discharge cycles, indicating that the structural change from the layered to spinel arrangement due to transition metal migration was more strongly curtailed. The respective charge-discharge profiles at various cycle numbers (Fig. 5e) firmly validate the above result. The differential capacity *(dQ/dV)* plots at different cycles were also analyzed to further authenticate this voltage decay (Fig. 5(f–h)). The discharge profiles of all three samples comprised three main voltage regions around 4.2 V, 3.6 V, and 3.0 V. The voltage region around 4. 2 V could be attributed to the presence of lithium at tetrahedral sites, while the peaks around 3.6 V are due to $Ni^{4+/3+}/Co^{4+/3+}$ redox couples, and the voltage peaks at 3.0 V are related to the-Mn^{4+}/Mn^{3+} redox pair. The peak at 3.0 V continuously shifted towards lower voltage upon cycling and finally appeared as a voltage peak around 2.50 V at the 200^{th} cycle for the undoped sample. Some shoulder peaks also appeared (marked by a circle) upon cycling, thus indicating the presence of the spinel phase. Similar trends were observed for the K^+-doped sample, although, to a lower extent. Comparatively, for the LKMNCOS sample, no remarkable change/splitting of the 3.0 V peak was observed, suggesting the absence of spinel traces during extended cycling. A voltage peak was observed at ~2.8 V in the discharge profile of the co-doped sample at the 200^{th} cycle, where the voltage was higher than that of the undoped and K^+-doped samples. However, the K^+/S^{2-}-doped sample also displayed a continuous shift of the 3.0 V peak towards lower voltage values, as predicted by the charge-discharge profiles, suggesting that slight structural deformations were still present and could not be eliminated completely. Overall, the rate and cycling performance indicate that the co-doping strategy is highly effective for delaying structural deformation and preventing transition metal migration.

3.4. Structural changes during charge/discharge

To validate the outstanding rate and cycling performance, the structural variations in the optimized samples during lithium deinsertion/insertion were evaluated by ex-situ XRD measurements. Fig. 6 shows the X-ray diffractograms measured for different states of charge and discharge at 0.1 C-rate. The cells were first charged to 4.8 V and then discharged to 2.0 V at the same current rate. As shown in Fig. 7, for all of the optimized compositions, the typical XRD profile of the hexagonal α-$NaFeO_2$ unit cell with *R-3m* symmetry was maintained. The magnified view of the (003) peak

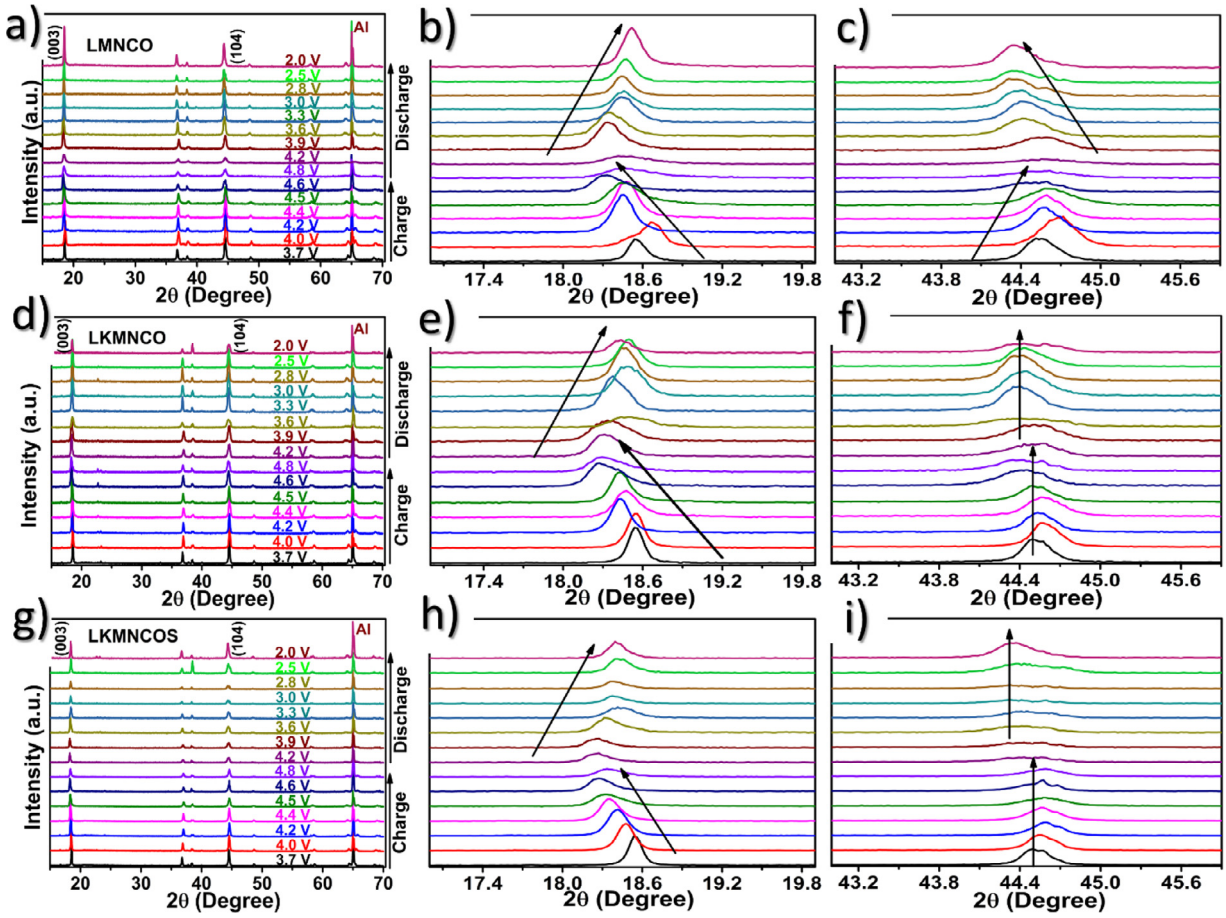

Fig. 6. Ex-situ XRD results of optimized samples at different state of charge and discharge, when cycled at 0.1 C-rate, and corresponding enlarged view of two major peaks [(003) and (104)].

for all samples showed almost similar changes. During charging, the (003) peak at ~19° shifted towards lower 2θ angles (Fig. 6b), while during discharging, the peak shifted to the right (i.e., higher 2θ angles), indicating continuous expansion and contraction along the *c*-axis, which is in good agreement with the previous reports for lithium-rich cathodes [49]. Expansion and contraction of the *c*-axis during lithium removal (charging) and insertion (discharging) are clearly expected as this process leads to the repulsion between the oxygen layers, which are shielded by the presence of lithium atoms. The changes in the (104) peak followed different trend for the pristine and doped samples. As observed from the expanded view (Fig. 6c), the (104) peak at ~45° followed the opposite trend to that observed for the (003) peak of LMNCO, i.e., during deinsertion, the (104) peak shifted towards higher 2θ angles, while during insertion, the peak shifted towards lower 2θ angles. However, for the K^+ and K^+/S^{2-}-doped samples, the (104) peak changed minimally during charge-discharge. This could be explained on the basis of rearrangement of the transition metal (TM) ions during charge-discharge. The removal of lithium during charging also leads to migration of the transition metal (Ni^{2+}) to the vacancies created by lithium, which leads to irreversible volume expansion and contraction of the microstructure as evident in the case of LMNCO (Scheme 2). However, for the K^+/S^{2-}-doped samples, the position of the (104) peak remained unchanged, indicating robustness of the crystal structure during charging-discharging. The presence of K^+ and S^{2-} ions in the doped samples is, therefore, believed to provide support to maintain a rigid layered structure by hindering transition metal ion migration at the lithium sites, which in turn leads to a stable reversible structure during lithium insertion and removal (Scheme 2). This explanation is firmly supported by the work reported separately on cation and anion-doping in previous reports [2,28]. To further verify this postulate, the structural changes of the optimized samples were examined at different cycle numbers for the pristine, K^+-doped, and K^+/S^{2-}doped samples at 1.0 C-rate; the obtained XRD patterns are shown in Fig. 7. For the undoped lithium-rich sample, the (003) and (104) peaks were split after the 2nd charge-discharge and remained apparent in the subsequent cycles. A shoulder peak appeared after the 2nd cycle and gained intensity at the expense of the main peak, which shifted continuously towards lower 2θ values. Similarly, (003)/(104) peak splitting was observed for the K^+-doped sample; however, the onset of splitting was delayed, becoming apparent at the 10th cycle. This indicates that the irreversible structural changes due to transition metal migration during lithium insertion/extraction are more pronounced in the pristine sample than in the K^+-doped sample. This difference indicates that doping with a larger cation hindered changes in the crystal structure during repeated cycling to some extent. However, during prolonged cycling, this effect is overridden by other multiple factors such as Jahn-Teller distortion, which comes into play from a disproportionation reaction involving splitting of Mn^{3+} to Mn^{4+} and Mn^{2+} [50]. The thus-formed Mn^{2+} species favor tetrahedral sites over octahedral sites, leading to spinel-type structures and hence, lower structural stability. On the other hand, for the co-doped sample, no splitting of the (003)/(104) peaks and/or any secondary phase was observed even after the 100th cycle at 1.0 C-

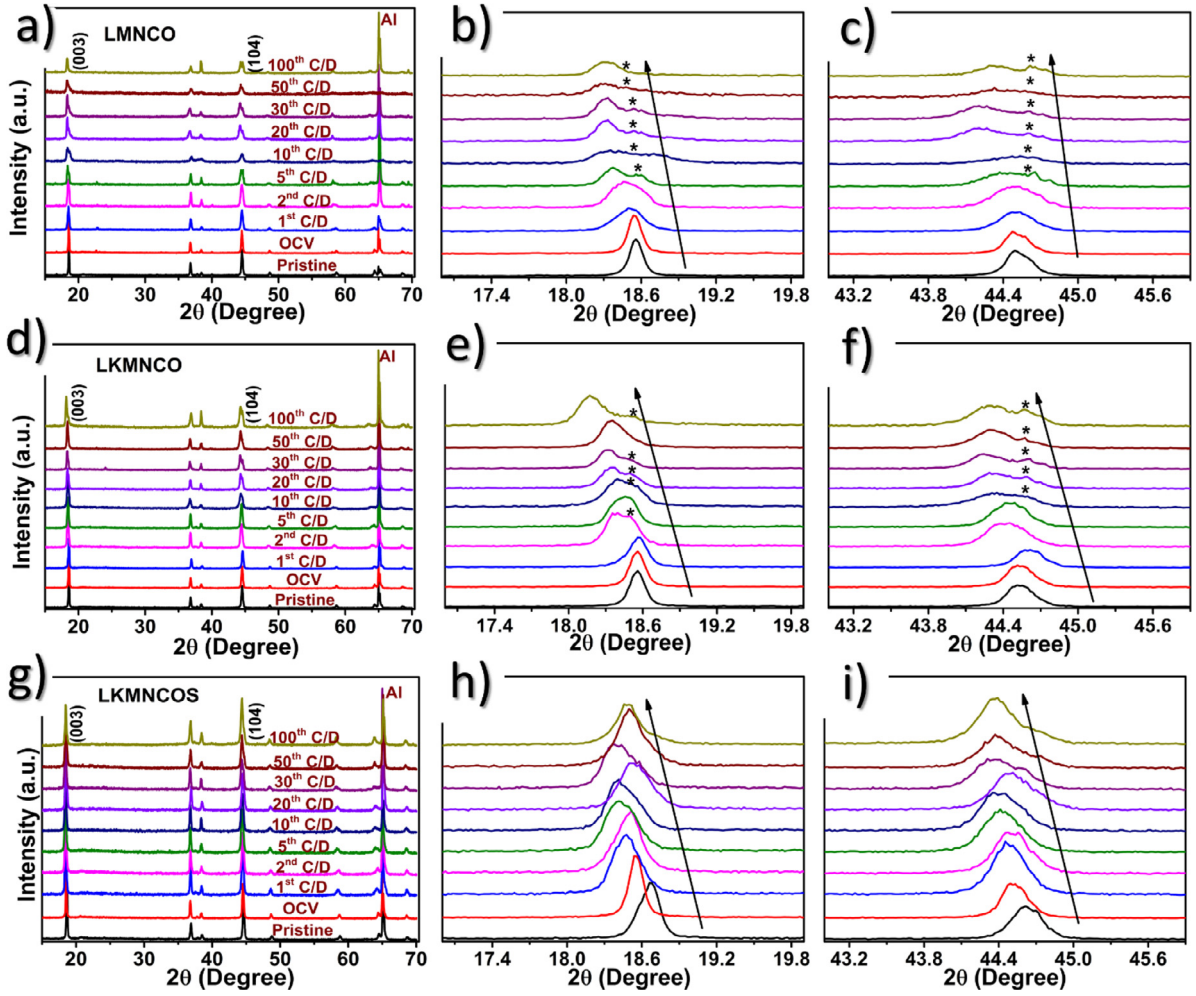

Fig. 7. Ex-situ XRD results of optimized samples at various cycle number cycled at 1.0 C-rate, and corresponding enlarged view of two major peaks [(003) and (104)].

rate. This suggests that co-doping not only supports structural reversibility, but also prohibits transition metal ion migration to the lithium sites. The presence of a larger cation (K^+ in the present case) at few lithium sites hinders formation of the spinel structure in the fixed closely packed oxygen framework. These results are well supported by the work of Mai et al., where they investigated $K_{0.7}Fe_{0.5}Mn_{0.5}O_2$, $Na_{0.7}Fe_{0.5}Mn_{0.5}O_2$, and $Li_{0.7}Fe_{0.5}Mn_{0.5}O_2$ as layered cathodes and systematically proved that the K[TM]O_2 framework is superior in terms of structural robustness, reversibility, and cyclability than the Na/Li isostructural framework [51]. In addition, structural damage to the lithium-rich cathodes is inevitable due to instability in the oxygen layers caused by the oxygen release during the initial charge process [52-54]. The collapse of oxygen layer gradually increases the deterioration of layered structure. Therefore, the presence of a larger anion (S^{2-}) in the oxygen framework can be treated as an inactive pillars that help to stabilize the layered structure by suppressing the formation of oxygen vacancy by weakening the interaction of oxygen and metal atoms as previously reported [2]. In addition, enlarging interlayer spacing subsequently lowers the energy barrier required for the smooth Li-ion insertion and extraction. Therefore, the presence of both K^+ and S^{2-}, along with transition metals, can be envisaged as a prototype similar to the K[TM]S_2 system, which is superior to the Li counterparts in terms of the electrochemical properties [55]. Hence, the synergetic effects of co-doping are believed to inhibit structural collapse and thus provide better lithium kinetics and electrochemical performance, as evidenced by the cycling and rate capability results.

3.5. Diffusion coefficient and Impedance analysis

GITT was employed to confirm the Li^+ diffusion kinetics during charge-discharge (C/D); the results are presented in Fig. 8(a, c, e). The GITT measurement was performed at a current pulse equivalent to 0.1 C for 30 min, followed by a relaxation period of 2 h. The lithium-ion chemical diffusion coefficients (D_{Li+}) for all the optimized samples were calculated using Eq. (1).

$$D = \frac{4}{\pi \tau}\left(\frac{n_m V_m}{S}\right)\left(\frac{\Delta E_s}{\Delta E_t}\right)^2 \quad (1)$$

In Eq. (1), V_m is the molar volume ($cm^3\ mol^{-1}$), τ is the duration of the applied current pulse (s), n_m and S are the number of moles and electrode surface area, respectively, and ΔE_s is the change in the steady-state voltage after a current pulse; ΔE_t represents the voltage change during a current pulse (Fig. S10) [56]. As shown in Fig. 8, the curves display higher D_{Li+} values during charge and discharge for LKMNCO and LKMNCOS samples compared to the pristine LMNCO sample. The average D_{Li+} value of 1.02×10^{-10} $cm^2\ s^{-1}$ during charge for LKMNCOS is 2.43 times higher than the bare LMNCO sample (0.42×10^{-10} $cm^2\ s^{-1}$). Likewise, the average D_{Li+} value of 1.30×10^{-10} $cm^2\ s^{-1}$ during discharge for co-doped LKMNCOS sample is 1.35 times higher than the bare LMNCO sample (0.96×10^{-10} $cm^2\ s^{-1}$). As apparent, the lithium diffusion coefficient was higher for the K^+/S^{2-}-doped sample owing to enlargement of the interlayer spacing and the better ability to maintain a robust-reversible layered structure even after

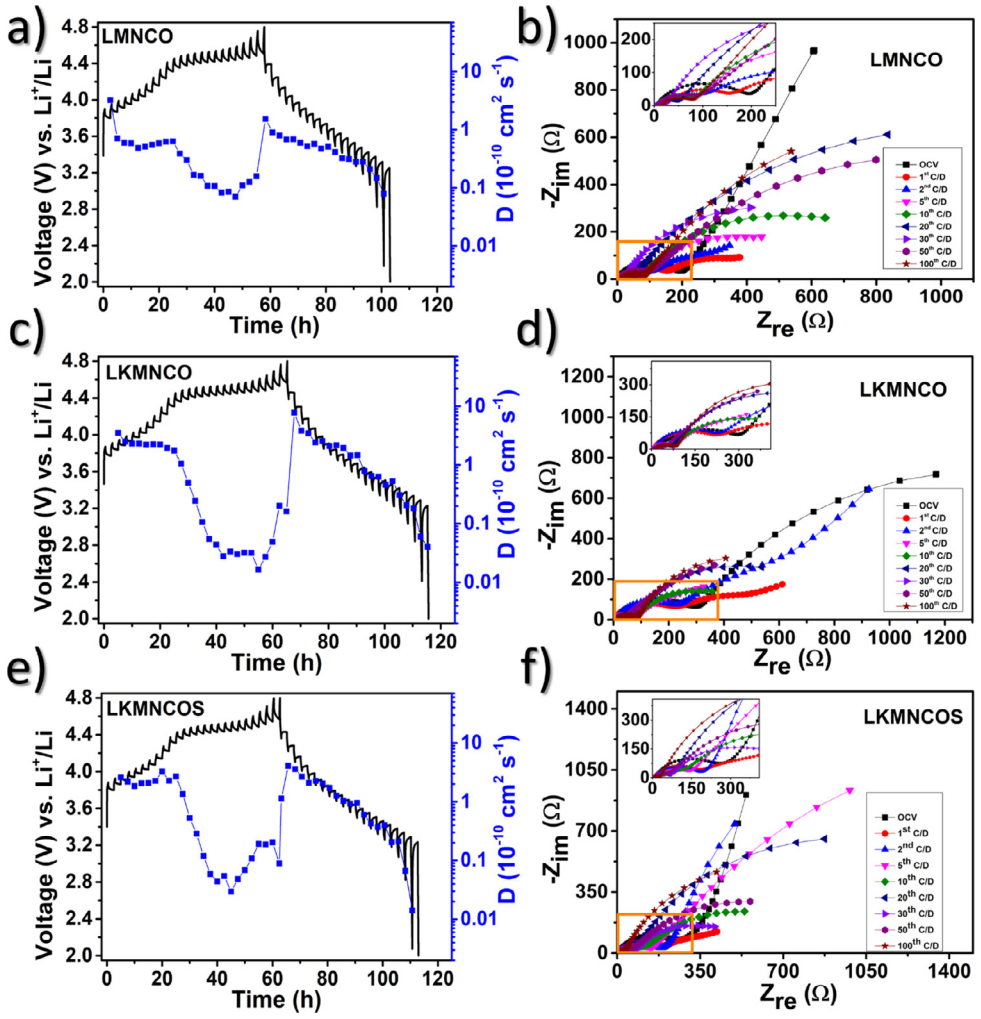

Fig. 8. Lithium-ion diffusion coefficient (D_{Li+}) measurements using GITT curves during charge-discharge. (a, c, e) GITT curves of LMNCO, LKMNCO, and LKMNCOS samples. GITT was performed at a current pulse equivalent to 0.1 C for 30 min followed by a relaxation of 2 h, (b, d, f) EIS measurements of the optimized samples at various cycle number during cycling at 1.0 C-rate.

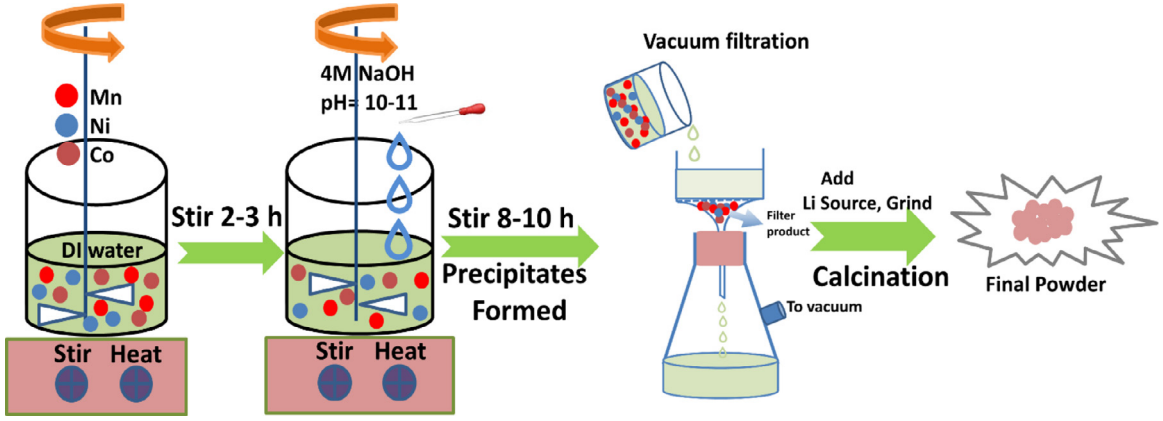

Scheme 1. Schematic illustration of synthesis process for Li-rich layered-type cathode materials.

prolonged cycling. Additionally, the obtained D values are in good accordance with the previously reported results for Li^+ diffusion [2]. Therefore, the improved D_{Li+} values during charge and discharge clearly indicate that the synchronized incorporation of K^+ and S^{2-} effectively improves the diffusion kinetics by simultaneously enlarging the interlayer spacing and prohibiting transitional metal migration to the lithium sites (Scheme 2).

Electrochemical impedance spectroscopy (EIS) measurements were performed to evaluate the kinetics and behavior at the interface inside the assembled cells. EIS data were obtained at different cycle numbers during charge/discharge at 1.0 C-rate, as shown in Fig. 8(b, d, f). As evident from the EIS curves, for all samples, the charge transfer resistance (R_{ct}, depressed semicircle in the high-medium frequency region) decreased, with in-

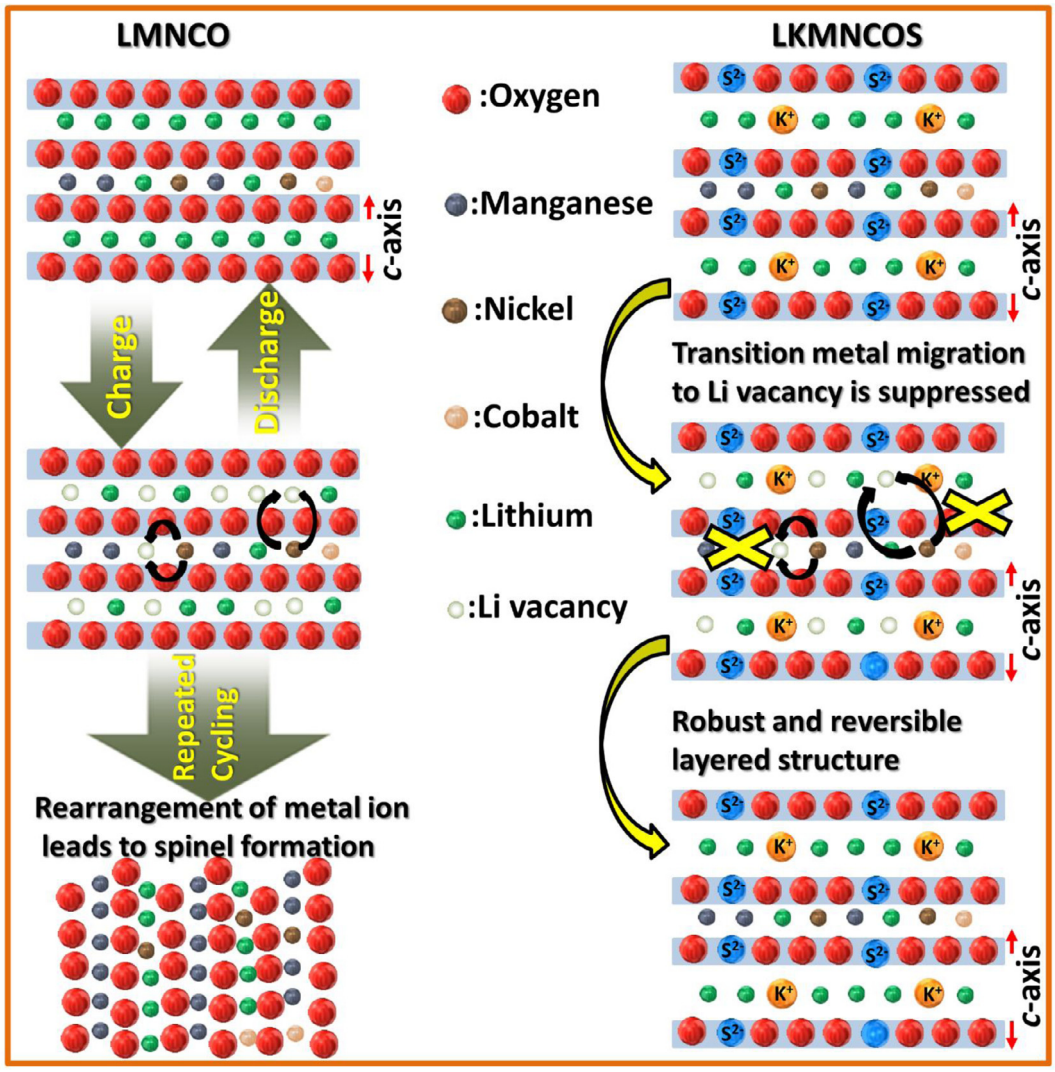

Scheme 2. Schematic illustration of synergetic effects induced by co-doping of larger cation/anion to enhance the structural stability and therefore, improvement in the electrochemical performance of co-doped LKMNCOS sample for long-lasting advanced lithium-ion batteries.

creasing cycling. However, after 100 cycles, the R_{ct} was lowest (~25 Ω) for the K^+/S^{2-}-doped sample, i.e., LKMNCOS, with higher values (~70-80 Ω) for the LMNCO and LKMNCO samples. The solution resistance (R_s, first intercept at the real x-axis by the semicircle in the high-frequency region) for all the assembled cells varied over cycling, indicating slightly different electrode-electrolyte environment inside the cells. The R_s for the cell with the LMNCO cathode was slightly higher after 100 cycles than for those with the K^+-doped and K^+/S^{2-}-doped cathodes. This is attributed to the formation of a stable electrolyte interface between the electrode-electrolyte in the doped samples. The obtained EIS data are well synchronized with the diffusion coefficients (D_{Li+}) determined by GITT analysis and the cycling/rate performance. These results again confirm that the improved structural properties, enlarged lithium channels, and effective mitigation of the layered-to-spinel structural transformation significantly enhanced the Li^+-ion kinetics. Finally, we believe that the adopted K^+ and S^{2-}-doping strategy could provide solutions for addressing various limitations of Li-rich cathodes such as structural deformation, voltage decay, and inferior cycling/rate performance. The obtained results and corresponding explanations could open up new avenues for the development of hybrid cathodes for advanced lithium-ion batteries.

4. Conclusions

In summary, we utilized a co-doping approach to overcome structural and electrochemical shortcomings of Li-rich layered cathode material. The optimized $Li_{1.135}K_{0.03}MNCOS_{0.02}$ (LKMNCOS) sample, display enhanced electrochemical performance with exceptional structural stability. The synthesized LKMNCOS sample delivered a stable discharge capacity of 217.0 mAh g^{-1} at the end of the 80th cycle at 0.1 C-rate. In addition, co-doped sample exhibits lowest average capacity decay rate per cycle (~0.07%) at 1.0 C, suggesting excellent cycling performance. The rate performance was also noteworthy as the LKMNCOS sample delivers high discharge capacities of 246, 218, 188, 155, 129, 93, and 80 mAh g^{-1} at 0.1, 0.2, 0.5, 1.0, 2.0, 5.0, and 7.0 C-rates, respectively. The excellent electrochemical performance of the co-doped sample could be attributed to the exceptional structural stability, hinderance for layered to spinel transformation, effective prevention of transition metal migration to the Li-sites, and stable oxygen layer or reduced irreversible capacity loss (ICL). Overall, the present work provides a novel interpretation of layered-spinel intergrowth and a mechanism to further stabilize the layered structure using the co-doping approach. Therefore, the knowledge gained in the present work could open new frontiers and deliver appropriate direction in the

development of advanced layered cathode materials with extraordinary cycling and rate performance.

Declaration of Competing Interest

None.

Credit authorship contribution statement

Rakesh Saroha: Visualization, Investigation, Methodology, Data curation. **Jung Sang Cho:** Conceptualization, Data curation, Writing - review & editing. **Jou-Hyeon Ahn:** Conceptualization, Supervision.

Acknowledgments

This work was supported by National Research Foundation of Korea (NRF) grant funded by the Korean Government (MSIT) (NRF-2017M1A2A2087577 and 2020M1A2A2038319).

Supplementary materials

Supplementary material associated with this article can be found, in the online version, at doi:10.1016/j.electacta.2020.137471.

References

[1] R. Saroha, A. Gupta, A.K. Panwar, Electrochemical performances of Li-rich layered-layered Li_2MnO_3-$LiMnO_2$ solid solutions as cathode material for lithium-ion batteries, J. Alloys Compd 696 (2017) 580–589.
[2] G. Chen, J. An, Y. Meng, C. Yuan, B. Matthews, F. Dou, L. Shi, Y. Zhou, P. Song, G. Wu, Cation and anion Co-doping synergy to improve structural stability of Li-and Mn-rich layered cathode materials for lithium-ion batteries, Nano Energy 57 (2019) 157–165.
[3] H. He, L. Zan, J. Liu, Y. Zhang, Template-assisted molten-salt synthesis of hierarchical lithium-rich layered oxide nanowires as high-rate and long-cycling cathode materials, Electrochim. Acta 333 (2020) 135558.
[4] X. Jiang, B. Wu, X. Yang, K. Xiong, Q. Liu, Y. Zhang, H. Shu, P. Gao, S. Xu, X. Wang, Multiple regulation of surface engineering for lithium-rich layered cathode materials via one-step strategy, Electrochim. Acta 325 (2019) 134951.
[5] B. Deng, Y. Chen, P. Wu, J. Han, Y. Li, H. Zheng, Q. Xie, L. Wang, D.-L. Peng, Lithium-rich layered oxide nanowires bearing porous structures and spinel domains as cathode materials for lithium-ion batteries, J. Power Sources 418 (2019) 122–129.
[6] Q. Liu, H. Zhu, J. Liu, X. Liao, Z. Tang, C. Zhou, M. Yuan, J. Duan, L. Li, Z. Chen, High-performance lithium-rich layered oxide material: effects of preparation methods on microstructure and electrochemical properties, Materials 13 (2020) 334.
[7] M. Xu, Z. Chen, H. Zhu, X. Yan, L. Li, Q. Zhao, Mitigating capacity fade by constructing highly ordered mesoporous Al_2O_3/polyacene double-shelled architecture in Li-rich cathode materials, J. Mater. Chem. A 3 (2015) 13933–13945.
[8] Z. Chen, X. Yan, M. Xu, K. Cao, H. Zhu, L. Li, J. Duan, Building honeycomb–like hollow microsphere architecture in a bubble template reaction for high-performance lithium-rich layered oxide cathode materials, ACS Appl. Mater. & Interfaces 9 (2017) 30617–30625.
[9] Y. Zhu, N. Zhang, L. Zhao, J. Xu, Z. Liu, Y. Liu, J. Wu, F. Ding, Improving electrochemical performance of lithium-rich cathode material $Li_{1.2}Mn_{0.52}Ni_{0.13}Co_{0.13}W_{0.02}O_2$ coated with Li_2WO_4 for lithium ion batteries, J. Alloys Compd 811 (2019) 152023.
[10] V.-C. Ho, S. Jeong, T. Yim, J. Mun, Crucial role of thioacetamide for ZrO_2 coating on the fragile surface of Ni-rich layered cathode in lithium ion batteries, J. Power Sources 450 (2020) 227625.
[11] G. Hu, Z. Xue, Z. Luo, Z. Peng, Y. Cao, W. Wang, Y. Zeng, Y. Huang, Y. Tao, T. Li, Z. Zhang, K. Du, Improved cycling performance of CeO_2-inlaid Li-rich cathode materials for lithium-ion battery, Ceram. Int. 45 (2019) 10633–10639.
[12] L. Wu, X. Tang, Z. Rong, X. Chen, J. Huang, T. Chen, X. Fang, Y. Wang, W. Dang, Studies on electrochemical reversibility of lithium tungstate coated Ni-rich $LiNi_{0.8}Co_{0.1}Mn_{0.1}O_2$ cathode material under high cut-off voltage cycling, Appl. Surf. Sci. 484 (2019) 21–32.
[13] P. Zou, Z. Lin, M. Fan, F. Wang, Y. Liu, X. Xiong, Facile and efficient fabrication of Li_3PO_4-coated Ni-rich cathode for high-performance lithium-ion battery, Appl. Surf. Sci. 504 (2020) 144506.
[14] Y. Li, F. Lai, X. Zhang, H. Wang, Z. Chen, X. He, Q. Li, Surface modification of Sr–doped $LaMnO_3$ coating by spray drying on Ni-rich $LiNi_{0.8}Mn_{0.1}Co_{0.1}O_2$ cathode material for lithium-ion batteries, J. Taiwan Inst. Chem. E. 102 (2019) 225–232.
[15] J. Wang, J.Y. Li, Z.B. Shao, H.T. Fan, H.Q. Ru, S.Y. Zang, One-pot preparation of $LiFePO_4$/C, Korean J. Chem. Eng. 36 (2019) 281–286.
[16] B. Jiang, B. Luo, J. Li, P. Peng, J. Chen, L. Chu, Y. Li, M. Li, Electrochemical effect of graphite fluoride modification on Li-rich cathode material in lithium ion battery, Ceram. Int. 45 (2019) 160–167.
[17] R. Veena, J. Anbu Dinesh, S. Raman, P. Panigrahi, N. Ganapathi Subramaniam, Li and Mn-rich $Li_4Mn_5O_{12}$–Li_2MnO_3 composite cathode for next generation lithium-ion batteries, J, Energy Storage 24 (2019) 100754.
[18] J. Liu, Q. Liu, H. Zhu, F. Lin, Y. Ji, B. Li, J. Duan, L. Li, Z. Chen, Effect of different composition on voltage attenuation of Li-rich cathode material for lithium-ion batteries, Materials 13 (2020) 40.
[19] D. Xie, W. Zhou, K. Lin, C. Hu, P. Zheng, X. Hou, K.-h. Lam, Doping effect of fluoride anion on microstructural and electrochemical properties of lithium-rich cathode materials, Mater. Lett. 253 (2019) 82–85.
[20] Y.G. Sorboni, H. Arabi, A. Kompany, Effect of Cu doping on the structural and electrochemical properties of lithium-rich $Li_{1.25}Mn_{0.50}Ni_{0.125}Co_{0.125}O_2$ nanopowders as a cathode material, Ceram. Int. 45 (2019) 2139–2145.
[21] X. Lang, Y. Zhao, K. Cai, L. Li, D. Chen, Q. Zhang, A facile synthesis of stable TiO_2/TiC composite material as sulfur immobilizers for cathodes of lithium—sulfur batteries with excellent electrochemical performances, Energy Technol 7 (2019) 1900543.
[22] Z. Peng, K. Mu, Y. Cao, L. Xu, K. Du, G. Hu, Enhanced electrochemical performance of layered Li-rich cathode materials for lithium ion batteries via aluminum and boron dual-doping, Ceram. Int. 45 (2019) 4184–4192.
[23] B. Guo, J. Zhao, X. Fan, W. Zhang, S. Li, Z. Yang, Z. Chen, W. Zhang, Aluminum and fluorine co-doping for promotion of stability and safety of lithium-rich layered cathode material, Electrochim. Acta 236 (2017) 171–179.
[24] D. Liu, X. Fan, Z. Li, T. Liu, M. Sun, C. Qian, M. Ling, Y. Liu, C. Liang, A cation/anion co-doped $Li_{1.12}Na_{0.08}Ni_{0.2}Mn_{0.6}O_{1.95}F_{0.05}$ cathode for lithium ion batteries, Nano Energy 58 (2019) 786–796.
[25] H.S. Ko, H.W. Park, G.J. Kim, J.D. Lee, Electrochemical characteristics of lithium-excess cathode material ($Li_{1+x}Ni_{0.9}Co_{0.05}Ti_{0.05}O_2$) for lithium-ion batteries, Korean J. Chem. Eng. 36 (2019) 620–624.
[26] M. Eilers-Rethwisch, S. Hildebrand, M. Evertz, L. Ibing, T. Dagger, M. Winter, Comparative study of Sn-doped $Li[Ni_{0.6}Mn_{0.2}Co_{0.2-x}Sn_x]O_2$ cathode active materials (x = 0-0.5) for lithium ion batteries regarding electrochemical performance and structural stability, J. Power Sources 397 (2018) 68–78.
[27] M.N. Ates, Q. Jia, A. Shah, A. Busnaina, S. Mukerjee, K. Abraham, Mitigation of layered to spinel conversion of a Li-rich layered metal oxide cathode material for Li-ion batteries, J. Electrochem. Soc. 161 (2013) A290.
[28] Q. Li, G. Li, C. Fu, D. Luo, J. Fan, L. Li, K-doped LiMnCoNiO, a novel cathode material with an enhanced cycling stability for lithium-ion batteries, ACS Appl. Mater. Interfaces 6 (2014) 10330–10341.
[29] S. Dong, Y. Zhou, C. Hai, J. Zeng, Y. Sun, Y. Shen, X. Li, X. Ren, C. Sun, G. Zhang, Z. Wu, Understanding electrochemical performance improvement with Nb doping in lithium-rich manganese-based cathode materials, J. Power Sources 462 (2020) 228185.
[30] Z. Tai, W. Zhu, M. Shi, Y. Xin, S. Guo, Y. Wu, Y. Chen, Y. Liu, Improving electrochemical performances of Lithium-rich oxide by cooperatively doping Cr and coating Li_3PO_4 as cathode material for lithium-ion batteries, J. Colloid Interface Sci 576 (2020) 468–475.
[31] R.N. Ramesha, C.P. Laisa, K. Ramesha, Improving electrochemical stability by transition metal cation doping for manganese in lithium-rich layered cathode, $Li_{1.2}Ni_{0.13}Co_{0.13}Mn_{0.54-x}M_xO_2$ (M=Co, Cr and Fe), Electrochim. Acta 249 (2017) 377–386.
[32] C.P. Laisa, R.N. Ramesha, K. Ramesha, Enhanced electrochemical performance of lithium rich layered cathode materials by Ca^{2+} substitution, Electrochim. Acta 256 (2017) 10–18.
[33] L. Guo, X. Tan, S. Liu, J. Wu, J. Ren, T. Zhao, X. Kang, H. Wang, W. Chu, Considerable capacity increase of high-nickel lithium-rich cathode materials by effectively reducing oxygen loss and activating $Mn^{4+/3+}$ redox couples via Mo doping, J. Alloys Compd 790 (2019) 170–178.
[34] B. Song, M.O. Lai, Z. Liu, H. Liu, L. Lu, Graphene-based surface modification on layered Li-rich cathode for high-performance Li-ion batteries, J. Mater. Chem. A 1 (2013) 9954–9965.
[35] S. Pang, M. Zhu, K. Xu, X. Shen, H. Wen, Y. Su, G. Yang, X. Wu, S. Li, W. Wang, Enhanced electrochemical performance of $Li_{1.2}Mn_{0.54}Ni_{0.13}Co_{0.13}O_2$ via L-ascorbic acid-based treatment as cathode material for Li-ion batteries, J. Electrochem. Soc. 165 (2018) A1897.
[36] D. Li, Y. Sasaki, K. Kobayakawa, Y. Sato, structural Morphological, and electrochemical characteristics of $LiNi_{0.5}Mn_{0.4}M_{0.1}O_2$ (M=Li, Mg, Co, Al), J. Power Sources 157 (2006) 488–493.
[37] L. Baggetto, D. Mohanty, R.A. Meisner, C.A. Bridges, C. Daniel, D.L. Wood, N.J. Dudney, G.M. Veith, Degradation mechanisms of lithium-rich nickel manganese cobalt oxide cathode thin films, RSC Adv. 4 (2014) 23364–23371.
[38] L. Baggetto, N.J. Dudney, G.M. Veith, Surface chemistry of metal oxide coated lithium manganese nickel oxide thin film cathodes studied by XPS, Electrochim. Acta 90 (2013) 135–147.
[39] J. Meng, S. Zhang, X. Wei, P. Yang, S. Wang, J. Wang, H. Li, Y. Xing, G. Liu, Synthesis, structure and electrochemical properties of lithium-rich cathode material $Li_{1.2}Mn_{0.6}Ni_{0.2}O_2$ microspheres, RSC Adv 5 (2015) 81565–81572.
[40] S. Verdier, L. El Ouatani, R. Dedryvère, F. Bonhomme, P. Biensan, D. Gonbeau, XPS study on Al_2O_3-and $AlPO_4$-coated $LiCoO_2$ Cathode material for high-capacity Li ion batteries, J. Electrochem. Soc. 154 (2007) A1088.
[41] N. Venugopal, W.S. Kim, K.Y. Sohn, Room-temperature synthesis of Co3O4 nanoparticles self-assembled into meso/nanoporous microstructures and their application, Korean J. Chem. Eng. 36 (2019) 1536–1542.
[42] S.K. Martha, J. Nanda, G.M. Veith, N.J. Dudney, Surface studies of high voltage lithium rich composition: $Li_{1.2}Mn_{0.525}Ni_{0.175}Co_{0.}1O_2$, J. Power Sources 216 (2012) 179–186.

[43] Y. Sun, S. Wu, D.-H. Xia, L. Xu, J. Wang, S. Song, H. Fan, Z. Gao, J. Zhang, Z. Wu, Temperature dependence of passivity degradation on UNS N08800 in near neutral crevice chemistries containing thiosulphate, Corros. Sci. 140 (2018) 260–271.
[44] Y. Liu, D. Ning, L. Zheng, Q. Zhang, L. Gu, R. Gao, J. Zhang, A. Franz, G. Schumacher, X. Liu, Improving the electrochemical performances of Li-rich $Li_{1.20}Ni_{0.13}Co_{0.13}Mn_{0.54}O_2$ through a cooperative doping of Na^+ and PO_4^{3-} with Na_3PO_4, J. Power Sources 375 (2018) 1–10.
[45] T. Zhao, N. Zhou, X. Zhang, Q. Xue, Y. Wang, M. Yang, L. Li, R. Chen, Structure evolution from layered to spinel during synthetic control and cycling process of Fe-containing li-rich cathode materials for lithium-ion batteries, ACS Omega 2 (2017) 5601–5610.
[46] K.I. Hamad, Y. Xing, Stabilizing Li-rich NMC materials by using precursor salts with acetate and nitrate anions for Li-ion batteries, Batteries 5 (2019) 69.
[47] J. Pires, L. Timperman, A. Castets, J.S. Peña, E. Dumont, S. Levasseur, R. Dedryvère, C. Tessier, M. Anouti, Role of propane sultone as an additive to improve the performance of a lithium-rich cathode material at a high potential, RSC Adv. 5 (2015) 42088–42094.
[48] R. Saroha, A.K. Panwar, A. Gaur, Y. Sharma, V. Kumar, P.K. Tyagi, Electrochemical studies of novel olivine-layered ($LiFePO_4$-Li_2MnO_3) dual composite as an alternative cathode material for lithium-ion batteries, J. Solid State Electrochem 22 (2018) 2507–2513.
[49] J. Li, R. Shunmugasundaram, R. Doig, J.R. Dahn, In situ X-ray diffraction study of layered Li–Ni–Mn–Co Oxides: effect of particle size and structural stability of core–shell materials, Chem. Mater. 28 (2016) 162–171.
[50] Z.M. Chan, D.A. Kitchaev, J.N. Weker, C. Schnedermann, K. Lim, G. Ceder, W. Tumas, M.F. Toney, D.G. Nocera, Electrochemical trapping of metastable Mn^{3+} ions for activation of MnO_2 oxygen evolution catalysts, Proc. Natl. Acad. Sci. USA 115 (2018) E5261–E5268.
[51] X. Wang, P. Hu, C. Niu, J. Meng, X. Xu, X. Wei, C. Tang, W. Luo, L. Zhou, Q. An, New-type $K_{0.7}Fe_{0.5}Mn_{0.5}O_2$ cathode with an expanded and stabilized interlayer structure for high-capacity sodium-ion batteries, Nano Energy 35 (2017) 71–78.
[52] J. An, L. Shi, G. Chen, M. Li, H. Liu, S. Yuan, S. Chen, D. Zhang, Insights into the stable layered structure of a Li-rich cathode material for lithium-ion batteries, J. Mater. Chem. A 5 (2017) 19738–19744.
[53] B. Qiu, M. Zhang, L. Wu, J. Wang, Y. Xia, D. Qian, H. Liu, S. Hy, Y. Chen, K. An, Gas-solid interfacial modification of oxygen activity in layered oxide cathodes for lithium-ion batteries, Nat. Commun. 7 (2016) 1–10.
[54] C.J. Hansen, J.J. Zak, A.J. Martinolich, J.S. Ko, N.H. Bashian, F. Kaboudvand, A. Van der Ven, B.C. Melot, J. Nelson Weker, K.A. See, Multielectron cation and anion redox in lithium-rich iron sulfide cathodes, J. Am. Chem. Soc. 142 (2020) 6737–6749.
[55] N. Naveen, W.B. Park, S.P. Singh, S.C. Han, D. Ahn, K.S. Sohn, M. Pyo, $KCrS_2$ cathode with considerable cyclability and high rate performance: the first K^+ stoichiometric layered compound for potassium-ion batteries, Small 14 (2018) 1803495.
[56] Y.-S. Lee, K.-S. Ryu, Study of the lithium diffusion properties and high rate performance of $TiNb_6O_{17}$ as an anode in lithium secondary battery, Sci. Rep. 7 (2017) 1–13.